2010-2600
51st AIAA/ASME/ASCE/AHS/ASC Structures, Structural Dynamics, and Materials (SDM) Conference, 12-15 April, Orlando, Florida, USA
2010 AIAA SDM Student Symposium

Bending Test of a Variable-Stiffness Fiber-Reinforced Composite Cylinder

Adriana W. Blom*
Delft University of Technology, Delft, 2629HS, The Netherlands
Fokker Aerostructures, Papendrecht, 3351LB, The Netherlands

Mostafa Rassaian†
The Boeing Company, Seattle, WA, 98108, U.S.A.

Patrick B. Stickler‡
The Boeing Company, Everett, 98204, U.S.A.

Zafer Gürdal§
Delft University of Technology, Delft, 2629HS, The Netherlands

Two carbon-fiber-reinforced composite cylinders were tested in bending. One cylinder, the baseline cylinder, consisted of 0°, 90° and ±45° plies, whereas the other cylinder, called the variable-stiffness cylinder, contained plies with fiber orientations that varied in the circumferential direction, which caused a variation in laminate stiffness. The cylinders were optimized for maximum buckling load carrying capability under bending.[1] Simulations showed that the variable-stiffness cylinder was able to redistribute the applied loads around the circumference, resulting in lower strain values at both the tension and the compression side of the cylinder and an improvement of the buckling load by 18 percent compared to the baseline cylinder. The purpose of the bending test was to show that the improvements obtained in the analytical results could also be achieved experimentally. The baseline cylinder was tested first to serve as a benchmark for the variable-stiffness cylinder. The finite element model was adjusted based on the baseline cylinder tests to represent the experimental conditions correctly. The model took into account the flexible connection between the cylinder and the test fixture, the test mechanism and geometric imperfections present in the cylinder and showed good agreement with the experimental results. The variable-stiffness cylinder was tested twice: first oriented in the direction it was designed for and later rotated 180 degrees about the cylinder axis, such that the loading direction on the cylinder was reversed. The predicted global response and strain distributions for both configurations corresponded well with the experimental data. The flexible boundary conditions and the geometric imperfections affected the load and strain distributions of the baseline and the variable-stiffness cylinders, but the relative improvements of the variable-stiffness cylinder in the preferred orientation with respect to the baseline cylinder were not affected. Follow-up tests of the cylinders including cutouts or induced damage are planned in the future.

Nomenclature

E_x Laminate stiffness in axial direction, MPa
I Moment of inertia, m^4

*PhD Student, Aerospace Engineering, Member
†Technical Fellow, The Boeing Company
‡Technical Fellow, The Boeing Company
§Professor, Aerospace Engineering, Associate Fellow

k Spring stiffness, Nm^{-1}
L Cylinder length, m
M_{cr} Buckling moment, Nm
R Perfect cylinder radius, m
r Measured cylinder radius, m
T_i Fiber angle as design variable, deg
w Geometric imperfection in radial direction, mm
x Axial coordinate, m
z Vertical coordinate, perpendicular to the bending axis, m
Exp Experimental
FE Finite element
Riks Riks analysis

Subscripts

b Baseline
c Clamped boundary conditions
f Flexible boundary conditions
p Preferred loading orientation
r Reversed loading orientation
v Variable-stiffness

Symbols

θ Circumferential coordinate, deg
ε In-plane strain, μm/m
φ Fiber orientation angle, deg

I. Introduction

The use of fiber-reinforced composite laminates in commercial airframe structures has increased dramatically with the development of automated manufacturing processes such as advanced fiber placement (AFP) and tape laying and this is reflected in the amount of composites used in the Boeing 787 and the Airbus A350, close to 50 percent of the total structural weight.[2] The directionality, high stiffness-to-weight ratio and possibility to integrate parts for fiber-reinforced composites have resulted in substantial weight savings compared to traditional aluminum structures. The large scale application of fiber-reinforced composites would not be possible without ongoing development of design and analysis tools. Many of these design and analysis tools, however, are built around materials databases and allowables for laminates consisting of combinations of $0\,^\circ$, $90\,^\circ$ and $\pm 45\,^\circ$ plies, which limit the freedom of the designer. The availability of automated manufacturing methods such as AFP allows for other fiber orientations than $0\,^\circ$, $90\,^\circ$ and $\pm 45\,^\circ$, and even for continuously varying fiber orientations within a single ply. The available design options are significantly increased, providing designers with opportunities to the increase structural performance or reduce the structural weight.

The use of curvilinear fibers to improve the tensile load carrying capacity of a plate with a central hole has been studied analytically by Hyer and Charette.[3] In their work the fiber orientations were designed to be aligned with the principal stress directions to provide a more effective load path around the hole compared to the straight-fiber counterpart. The resulting laminates outperformed the quasi-isotropic laminates in tension, but did not show any improvements in buckling load. Hyer and Lee[4] therefore focused on improving the buckling load of panels with a central hole. Substantial increases in buckling load were achieved, while simultaneously the tensile strength was improved. The most important mechanism behind the increased buckling loads was a redistribution of the loads from the unsupported edge hole to the supported edges. Similar improvements in buckling load and tensile strength capability have been found by Nagendra et al.[5] who used NURBS to define fiber angle variations.

The concept of a continuous, linear fiber angle variation along one direction within a ply to tailor the stiffness of a composite laminate was introduced by Gürdal and Olmedo.[6] The resulting laminates are called *variable-stiffness laminates*. In Gürdal and Olmedo the fiber angle variation is defined using a small number of parameters. A stiffness variation in the direction perpendicular to the applied load[7,8] resulted in improvements of up to 80 percent due to a redistribution of the primary loads from the center section of

the panel to the simply supported sides of the panel. This redistribution of loads was obtained by having a higher laminate stiffness at the edges of the panel than at the center, i.e. the fibers at the panel edges were more aligned with the loading direction than the fibers at the panel center. Two variable-stiffness panels were manufactured using a Cincinnati Milacron VIPER advanced fiber placement machine[9] and tested by Wu et al.[10,11]

After the first variable-stiffness panels were built, a second design study was performed in which genetic algorithms were used in combination with a Rayleigh-Ritz solver to optimize a 20 ply rectangular variable-stiffness panel under axial compression, subjected to manufacturing constraints.[12] Improvements of more than 60 percent compared to the optimum constant-stiffness designs were shown with no appreciable increase in weight. The best variable-stiffness design was manufactured with a VIPER fiber placement machine.[13] An experimental program for the rectangular variable-stiffness panels was led by Jegley,[14] who showed that experimental buckling loads were significantly higher than predicted. This was confirmed by Lopes et al.[15] who simulated the experiments with the ABAQUS finite element code.[16] They predicted the non-linear buckling load and the laminate strength according to the physically-based NASA LaRC04 failure criteria. In a follow-up study by Lopes et al.[17] residual thermal stresses induced by the curing process were included in the analysis, resulting in a close agreement between analytical and experimental buckling values.

Other efforts to improve the performance of composite panels by changing the internal fiber geometry have been made by Jones and Platts.[18] They applied a Michell structure geometry to reduce the stress concentrations around a pin-loaded hole and showed that considerable improvements were possible compared to panels made of 0/90 woven cloth.

In another study by Tosh et al.[19] and Li et al.[20,21]the principal stress vectors or alternatively the principal load paths were used to determine the fiber trajectories in composite panels with the objective to increase the panel strength. Structural tests showed that the specific strength of specimens with an open hole tested in tension increased by 62 percent,[19] while the bearing strength in bolted joints increased by 169 percent.[20] Panels with large cutouts that were reinforced by fibers following the maximum and minimum principal stress trajectories carried a shear load that was 37 percent higher compared to the quasi-isotropic baseline at a 3 percent weight penalty.[21]

Near-field material orthotropy distribution was used by Huang et al.[22,23] to maximize the strength of a composite plate with a hole based on the first-ply Tsai-Wu failure criterion. They showed that a laminate with a hole consisting of 6 identically steered plies doubled the load-carrying capacity of a $[0,\pm 45]_S$ laminate with a hole.

A series of theoretical studies by Alhajahmad et al.[24–26] focused on tailoring fuselage skin panels for pressure pillowing using curvilinear fibers. A nonlinear angle variation offered improvements of up to 26 percent for different aspect ratio panels compared to straight-fiber configurations due to a stress redistribution over the panel. In a follow-up study the work was expanded to panels with window cutouts,[25,26] where improvements in both strength and buckling performance were achieved.

The concept of tailoring material properties by varying fiber orientations with circumferential position in elliptical composite cylinders for the purpose of improving axial buckling capacity is discussed by Sun and Hyer.[27] The buckling capacity was improved by making the entire cylinder participate in the buckling deformations. The fiber angle variation with circumferential position was based on a simplified buckling analysis of circular composite cylinders. It was shown that improvements in buckling capacity could be achieved for both small and large cylinders, regardless of the boundary conditions applied. Moreover, material failure characteristics were not compromised by varying fiber orientation with circumferential position.

Possible performance improvements of thin circular cylindrical shells using the variable-stiffness concept have been examined by Tatting.[28] Stress analysis and initial buckling estimates were formulated for a general variable-stiffness cylinder to be used in optimization studies. Two cases of loading and stiffness variation on short cylinders were selected to investigate the possible areas of improvements that the variable-stiffness concept might offer over constant-stiffness structures. The first case considered was a cylinder with axial stiffness variation only, subject to constant loads of axial compression, pressure and torsion. The results for these load cases showed little improvement compared to traditional laminates, mainly due to the presence of a weak link area within the stiffness variation that carried the ultimate load. The second design problem involved a cylinder with a stiffness variation in circumferential direction subject to axial compression, pressure, torsion, bending or transverse shear. The most significant improvements in load-carrying capacity were found for cases that involve loads that also vary circumferentially, i.e. bending and shear forces. The stiffness variation of the optimal designs contribute to increased performance in two ways:

lowering the stresses in the critical areas through redistribution of the stresses; and providing a relatively stiff region that alters the buckling behavior of the structure.

A composite cylindrical shell with circumferentially varying fiber orientations was the subject of study by Wu.[29] The shell was intended to represent a fuselage section of an aircraft subjected to bending loads. As such the variable-stiffness cylinders were designed to resemble an I-beam, with 10 degree fiber angles in the keel and crown sections to resist bending and 45 degree fiber orientations on the side to resist shear in a $[\pm 45, \pm\theta]_S$ layup. A cylinder with constant thickness and a cylinder with overlaps were analyzed using STAGS finite element models and compared to an 8-ply quasi-isotropic baseline. The shell with overlaps showed improved buckling load capacity and higher bending stiffness for bending about the horizontal axis. No improvements were found for bending about the vertical axis. The constant-thickness shell did not show improved bending stiffness or buckling performance in either direction. The two variable-stiffness shells with the fiber angle varying from 10 degrees at the crown to 45 degrees at the side, back to 10 degrees at the keel were manufactured using an Ingersoll fiber placement machine[30] and will be tested in bending in the near future.

The concept of curvilinear fiber paths manufactured by AFP was extended to conical and cylindrical shells by Blom et al.[31] A 609 mm (24 inches) diameter cylinder in pure bending was optimized to carry a maximum load before the cylinder buckled, while manufacturing, stiffness and strength constraints were applied.[1] It was shown that the buckling load could be increased by approximately 18 percent compared to a baseline consisting of 0 °, 90 ° and ±45 ° plies.[32] Both the baseline and the variable-stiffness cylinder were manufactured using an Ingersoll fiber placement machine located at Boeing in Seattle. Subsequently the cylinders were subjected to a modal experiment to determine the eigenfrequencies and eigenmodes of the shells, and the responses were compared to the analytical predictions that were made using the commercial finite element program ABAQUS.[33] The experimental eigenfrequencies which were measured from 0 Hz up to a frequency of 1250 Hz matched the predicted eigenfrequencies within 5 percent. The location and the peaks of the physical responses in terms of displacement, velocity and acceleration frequency response functions of the finite element analysis also correlated well with the experimental results.

The objective of the research presented in this paper was to show that the improvements obtained in the analytical results could also be achieved experimentally. The variable-stiffness cylinder design will be discussed first and a summary on the mechanisms behind the improved buckling performance based on earlier analyses[1] will be given. Subsequently the test mechanism for the bending test, the data acquisition and the test procedure will be described. Then an adjustment of the finite element model will be discussed, this was done to reflect the experimental conditions correctly, based on the test of the baseline cylinder. Comparisons between the analytical and experimental results of the variable-stiffness cylinder will be based on this finite element model. The results for the tests of the variable-stiffness cylinder will be compared to the analytical results and to those of the baseline cylinder. Finally, conclusions about the accuracy of the finite element predictions and the performance of the variable-stiffness cylinder will be drawn and recommendations for future work will be made.

II. Cylinder with Stiffness Variation in the Circumferential Direction

The cylindrical shells considered in this paper consisted of 24 graphite-epoxy plies and had a radius of 304.8 mm (12 in). The length of the test section was 812.8 mm (32 in), while the total length of the cylinder is 990.6 mm (39 in). One cylinder, the *baseline* cylinder, had a conventional layup with 0 °, 90 °and ±45 °layers. The other cylinder contained plies with continuously varying fiber orientations resulting in a variable-stiffness laminate. This is referred to as the *variable-stiffness* cylinder. The layup of both shells resulted from an optimization for maximum bending load subjected to stiffness, strength and manufacturing constraints, as described by Blom et al.[1] The material used for manufacturing was slightly different from that used in the optimization described by Blom[1] and therefore the actual numbers of the optimal layups and buckling loads were also slightly different.

The layup of the baseline shell was: $[\pm 45, 0_2, 90_2, 0, \pm 45, \pm 45, 90]_S$. The layup of the variable-stiffness shell was a hybrid of fiber-steered plies and constant-angle plies. The steered plies had an angle variation in the circumferential direction, as shown in figure 1(a). The fiber angle φ was defined with respect to the longitudinal axis. The variation of the fiber angle within a ply was determined by a small number of design variables T_i, which fixed the fiber angle at 45 degree increments around the circumference, as shown in figure 1(b). The fiber orientations in-between these locations are defined by a constant curvature path, such that

the fiber angle varies as:

$$\cos\varphi(\theta) = \cos T_i + (\cos T_{i+1} - \cos T_i)\,\frac{\theta - \theta_i}{\theta_{i+i} - \theta_i} \tag{1}$$

where θ_i is the circumferential coordinate at which the fiber angle is defined by T_i. The bending load is symmetrical around the vertical plane and therefore the structure was also designed to be symmetric. This is shown in figure 1(b), where a cross-section of the shell is displayed with the design variables T_i spaced at 45 °increments around the circumference.

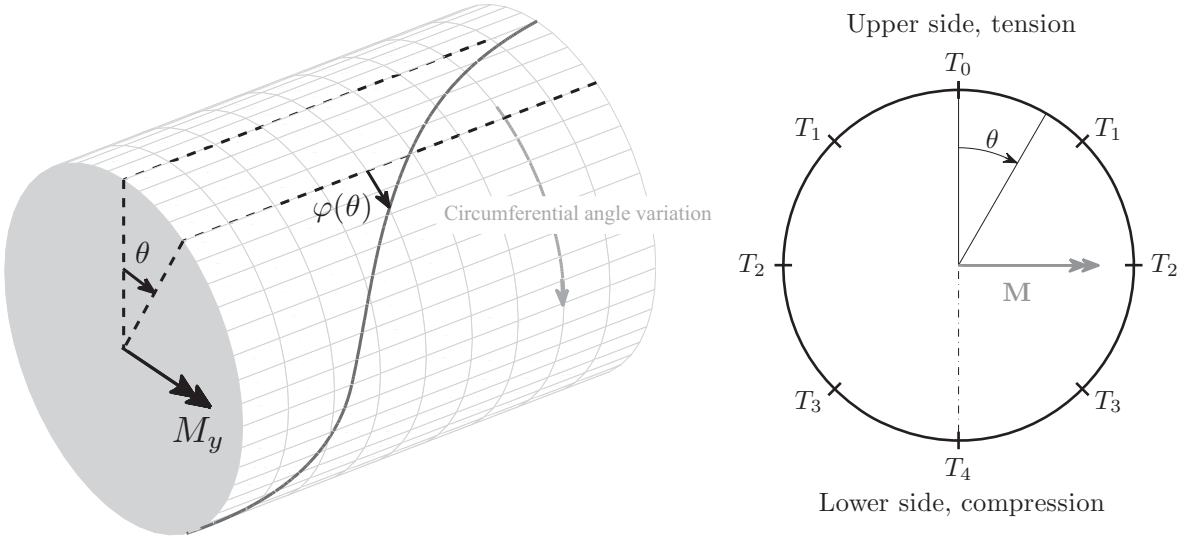

(a) Circumferential stiffness variation

(b) Definition of the design variables per ply

Figure 1. Schematic view of loading conditions and design parameters

The calculated buckling moment of the optimum variable-stiffness cylinder was 805 kNm, an improvement of 18 percent compared to the buckling moment of the baseline cylinder, which was 678 kNm. The improvement in buckling load was achieved by a redistribution of the load around the circumference due to the non-uniform stiffness variation in the circumferential direction. The layup of the variable-stiffness shell was $[\pm 45, \pm\varphi_1(\theta), 0, 90, \pm\varphi_3(\theta), 0, 90, \pm\varphi_5(\theta)]_S$, where $\varphi_1(\theta)$, $\varphi_3(\theta)$ and $\varphi_5(\theta)$ represent three different steered ply definitions. The design variables, T_0 to T_4, for each of the three steered plies are given in table 1. The fiber paths corresponding to these design variables are shown in figure 2, where both the paths corresponding to the positive and the negative fiber angle variations are plotted on the developed cylinder surface.

Table 1. Ply variables of variable-stiffness shell with layup $[\pm 45, \pm\varphi_1(\theta), 0, 90, \pm\varphi_3(\theta), 0, 90, \pm\varphi_5(\theta)]_S$

Ply	T_0 (°)	T_1 (°)	T_2 (°)	T_3 (°)	T_4 (°)
$\varphi_1(\theta)$	10.0	10.0	10.0	10.0	24.7
$\varphi_3(\theta)$	10.0	10.0	10.6	56.9	61.7
$\varphi_5(\theta)$	10.0	12.0	10.0	34.2	68.9

The variation of the axial stiffness with the circumferential coordinate is given in figure 3(a), where the stiffness of the variable-stiffness cylinder E_{xv} is normalized with the axial stiffness of the baseline cylinder E_{xb}. The axial stiffness on the tension side, between $\theta = 270\,°$ and $\theta = 90\,°$, was more than 80 percent larger than the stiffness of the baseline cylinder, while the stiffness on the compression side, near $\theta = 180\,°$, was slightly smaller than the stiffness of the baseline cylinder.

The bending moment was applied to the ends of the cylinder through rigid end plates and therefore the distribution of the axial load depended on the distribution of the axial stiffness. The load distributions of the baseline and the variable-stiffness cylinder are shown in figure 3(b), where three regions are highlighted. The high stiffness on the tension side of the variable-stiffness cylinder caused the loads in region A to be

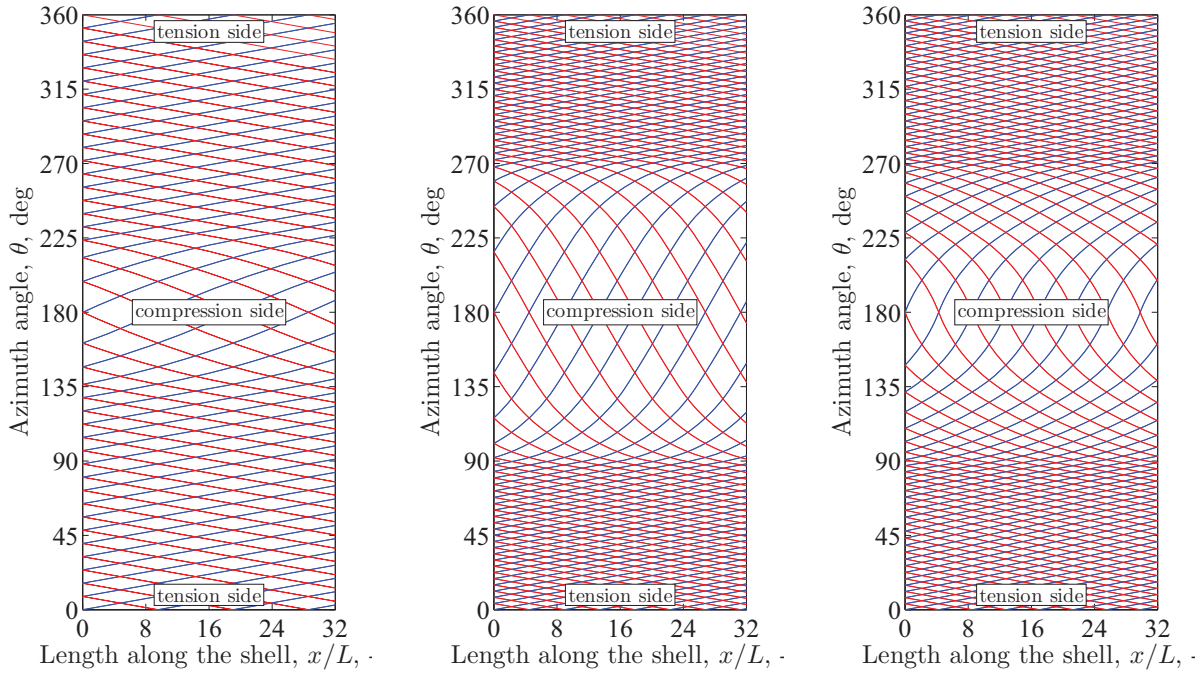

(a) $\pm\varphi_1(\theta)$ (b) $\pm\varphi_3(\theta)$ (c) $\pm\varphi_5(\theta)$

Figure 2. Ply angle variations in: $[\pm 45, \pm\varphi_1(\theta), 0, 90, \pm\varphi_3(\theta), 0, 90, \pm\varphi_5(\theta)]_S$

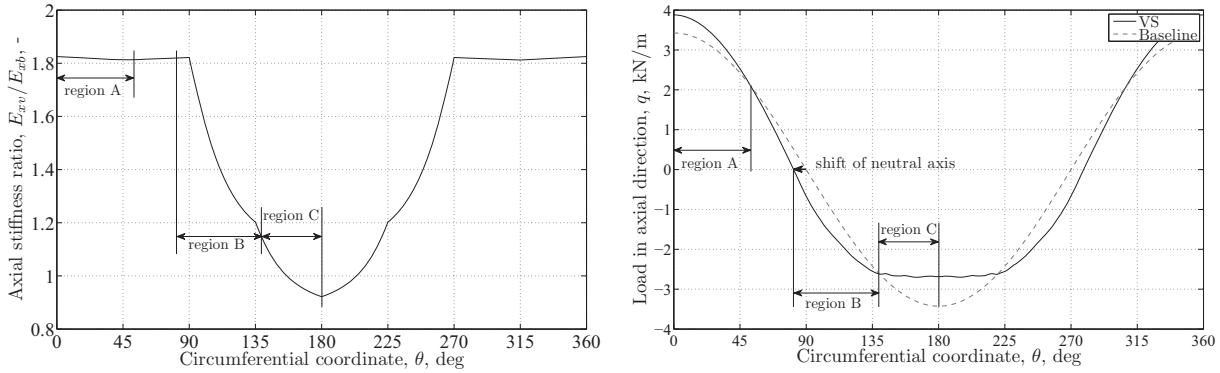

(a) Axial strain distribution (b) Axial load distribution

Figure 3. Load and stiffness distribution of the variable-stiffness cylinder

significantly larger than those of the baseline cylinder. Another consequence of the higher stiffness on the tension side is a shift of the neutral axis towards the tension side, i.e. the neutral axis shifted from $\theta = 90\,^\circ$ to $\theta = 81\,^\circ$. The shift in neutral axis resulted in all-compressive loads in region B for the variable-stiffness cylinder, whereas the compressive loads carried by the baseline cylinder in this region were much smaller or even tensile. The low axial stiffness of the variable-stiffness cylinder in region C resulted in a flattening of the load curve on the compression side of the cylinder, yielding compressive load values almost 20 percent smaller compared to the baseline cylinder.

The circumferential stiffness variation resulted in a redistribution of the loads, such that the tension side was more effective in carrying loads, the compressive loads were carried by a larger part of the cylinder and the compressive load peak at $\theta = 180\,^\circ$ was significantly reduced. The compressive side of the cylinder was critical for buckling, so redistributing the compressive loads over a larger portion of the cylinder and reducing the compressive peak load near $\theta = 180\,^\circ$ permitted a higher bending moment to be carried before buckling occurred.

The baseline and the variable-stiffness cylinders were manufactured by Boeing using an Ingersoll fiber

placement machine.[32] A picture of a steered ply during the manufacturing of the variable-stiffness cylinder is shown in figure 4.

Figure 4. The variable-stiffness cylinder during manufacturing

III. Test Setup, Data Acquisition and Test Procedure

A test fixture was designed exclusively for the bending tests of the cylinders, see figure 5. The setup resembled a 4-point bending setup, where the cylinder was mounted in the area where no shear force was present, such that the cylinder was subjected to pure bending. A 3,560 kN MTS test bench, model 311.51S, was used for the actuation. The bending loads were applied symmetrically to the cylinder by allowing the moment arms to rotate, with the rotation of the moment arms controlled by the vertical motion of the machine head. The force applied by the machine, and hence the bending moment applied to the shell, was measured using a load cell. The test fixture was loaded in tension, causing a bending moment such that the upper side of the cylinder was in tension and the lower side of the cylinder was in compression. The amount of undesired forces was minimized by the presence of pinned hinges, indicated in red in figure 5(b).

(a) Picture (b) Model

Figure 5. MTS Test bench with the bending fixture

The boundary conditions of the cylinder were designed to approach clamped end conditions using a bolted

connection with steel end reinforcements of the cylinder to improve the bearing capability of the laminate, see figure 6(a). Both ends of the cylinder were attached to a steel outer ring and a segmented steel inner ring, as shown in figure 6(b). The inner ring was segmented to enable clamping of the cylinder between the inner and outer ring, while paste adhesive was used as a filler material. The rings were bolted to rigid end plates which were integrated with the moment arms for the application of the bending moment.

(a) Cylinder before application of the speckle pattern

(b) Picture of the steel end rings

Figure 6. Cylinder and interface with the text fixture before assembly

The maximum load that could be applied to the cylinders was limited by the strength of the bolted connection which was most critical on the tension side of the variable-stiffness cylinder. Unfortunately the cylinders were built before the detailed design of the test fixture was done, resulting in cylinders that were expected to be too stiff to be buckled in the test section before bearing failure occurred on the tension side of the cylinder. It was thus decided to save the cylinders and not to load the cylinders beyond the load that would cause bearing failure. This would allow for a second test run that might include damage or cutouts in the test section to weaken the structure. The maximum design load based on the maximum bearing strength capacity was 415 kNm, approximately 65 percent of the calculated nonlinear buckling load of the baseline cylinder, or 55 percent of the buckling load of the variable-stiffness cylinder, the effect of geometric imperfections not included. The test fixture was sized according to the maximum load of 415 kNm.

The end rotations of the cylinders were measured indirectly by measuring the displacements of the end plates at two vertically spaced locations, see figure 7. Strains were measured at a number of locations on the cylinder surface, as indicated in figure 8, while the strains at one quarter of the cylinder were also measured with a digital image correlation (DIC) system which provided a full view of the strain field. The DIC system was also used to measure the geometric imperfections of the cylinders before they were assembled in the test fixture.

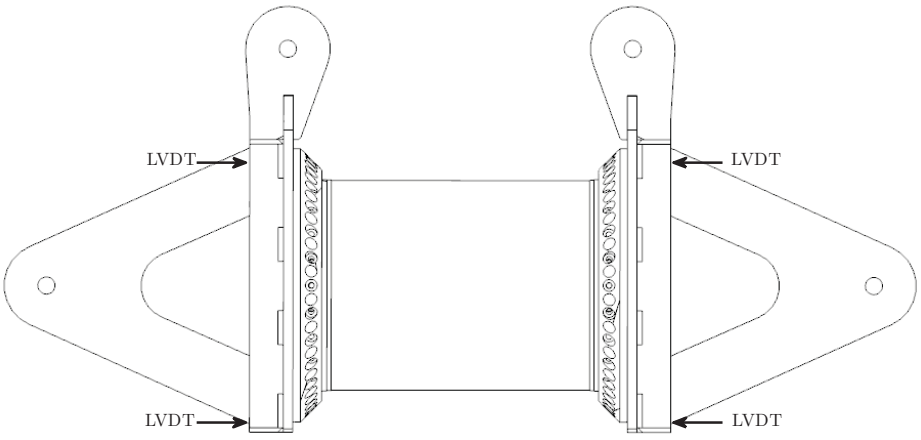

(a) Location of the LVDTs

(b) Picture of the LVDTs

Figure 7. Locations of the LVDTs for the measurement of the end rotations

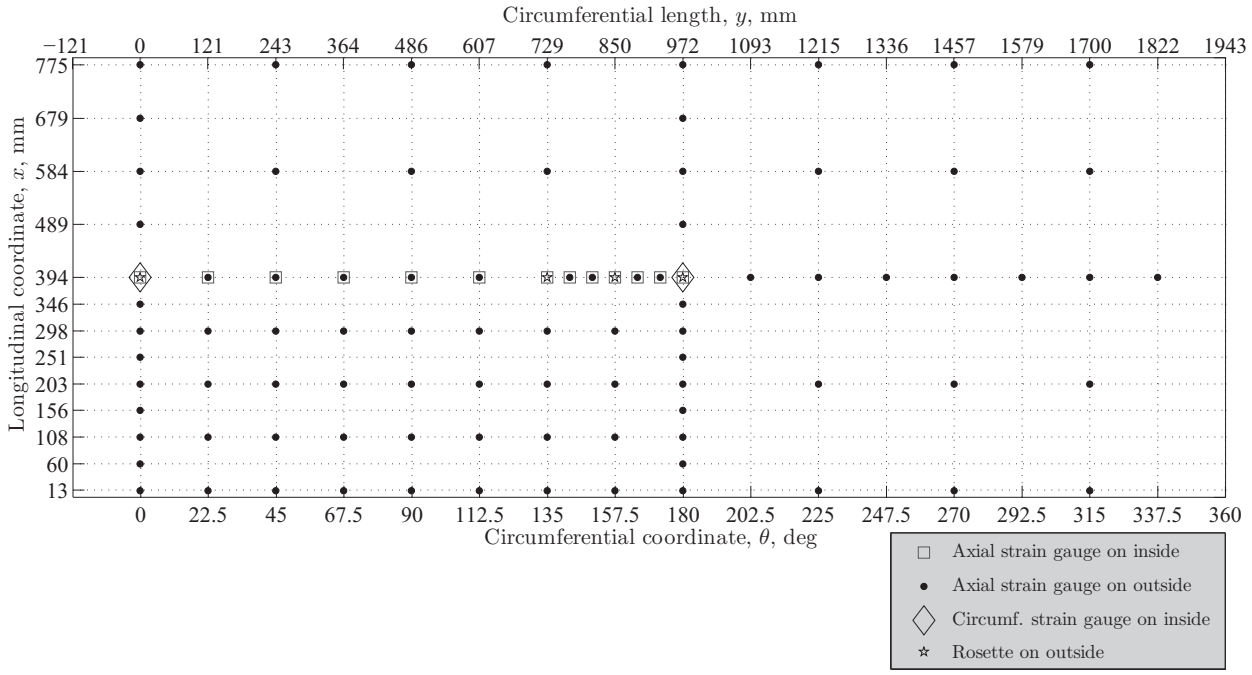

Figure 8. Location of strain gauges on the cylinder surface

The cylinders were loaded in steps of 10 kN force at the machine head, which corresponded to steps of 3.5 kNm bending moment, up to the maximum design load of 415 kNm. Strain and displacement data were collected at each load increment, and pictures were made using the DIC system. Multiple test runs were performed where the DIC system was first used to monitor the compression side of the cylinder, while the tension side of the cylinder was monitored in a subsequent run.

IV. Finite Element Predictions

The initial design of the baseline and the variable-stiffness cylinder was based on a linear bifurcation analysis using the finite element program ABAQUS. Structures often do not behave linearly, though, and test conditions usually deviate from simulated conditions, requiring adjustments of the finite element model. The baseline cylinder was used as a benchmark, such that the finite element model could be adjusted to reflect the test conditions correctly. The final model was then used to predict the test results of the variable-stiffness cylinder.

A. Linear and Nonlinear FE Models with Clamped Boundary Conditions

The finite element model used in the design phase was also used to predict the experimental response of the cylinder, except that the pre-buckling analysis was nonlinear instead of linear. The buckling load was calculated with a linear bifurcation analysis at a load slightly lower than the load at which the nonlinear pre-buckling analysis became unstable.

The moment-rotation curves for the experimental and the analytical results are shown in figure 9(a) and the distributions of the axial strain with the vertical coordinate $z = R\cos(\theta)$ are given in figure 9(b). The experimental results are denoted by "Exp" and the finite element results by "FE". The nonlinear finite element predictions with clamped boundary conditions are indicated with the subscript c: FE_c and are represented by the solid line. Two sets of experimental data are presented in the moment-rotation curve, which correspond to the end rotations at both ends of the cylinder. A difference of approximately 25 percent between the predicted and the measured bending stiffnesses can be observed when comparing the slopes of the experimental and analytical moment-rotation curves in figure 9(a), where the experimental response is more compliant than the predicted response. The difference in end rotations was expected to be caused by a difference in boundary conditions between the finite element model and the test, because a modal test of

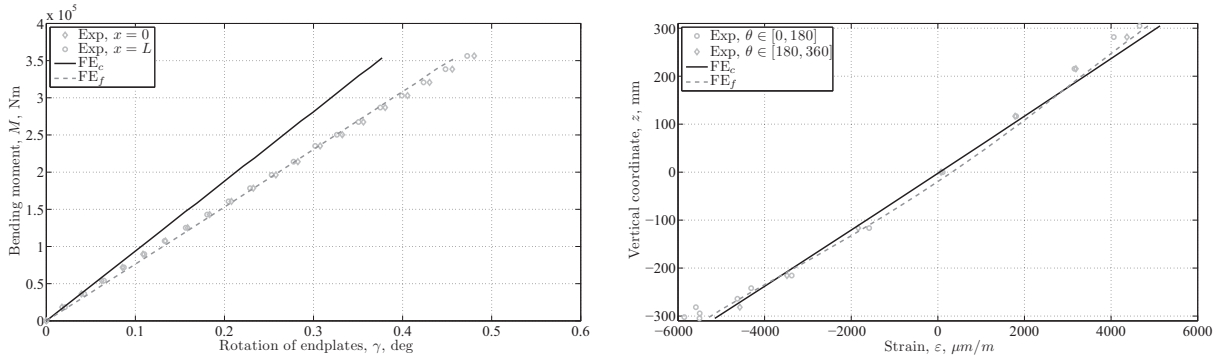

(a) Global response

(b) Strain distribution at M=356 kNm

Figure 9. Comparison baseline test and FE models with different boundary conditions

the cylinders[33] showed a good agreement between the experimental and analytical data, suggesting that the stiffness modeling was accurate.

The measured distribution of the axial strain with the vertical coordinate z halfway along the length of the cylinder, i.e. at $x = L/2$, supported this hypothesis. The distribution of the axial strain with the vertical coordinate z should have been linear if the boundary conditions were clamped:

$$\varepsilon = \frac{M_y z}{EI} \tag{2}$$

where M_y is the applied bending moment and EI is the bending stiffness of the cylinder. The strain distribution according to the finite element prediction in figure 9(b) was indeed a straight line. The experimental strain distribution, however, showed smaller strain values on the tension side and larger strain values on the compression side, indicating that the cylinder cross-section did not remain in one plane.

This observation was supported by data from the digital image correlation measurements. The rotations that were measured by the LVDTs were larger than the rotations that were measured by the DIC system, an indication of flexibility in the interface between the cylinder and the support structure. Furthermore, the rotations on the compression side as measured by the DIC system were larger than the rotations on the tension side, which was in line with the strain distribution of figure 9(b). An inspection of the load transfer mechanisms on the tension and compression side of the cylinder provided an explanation: on the tension side loads were transferred through the bolts and through shear at the cylinder-ring interfaces, whereas on the compression side loads were also transferred through direct contact between the back plate and the cylinder. The latter load transfer mechanism was more efficient and therefore the compression side of the cylinder was loaded higher than the tension side, causing larger strains on the compression side than on the tension side.

B. Nonlinear FE Model with Flexible Boundary Conditions and Mechanism

The large differences between the analytical response and the experimental response required an adjustment of the boundary conditions in the finite element model and thus linear springs were inserted between the cylinder ends and the rigid end plates. These springs were rigid in the plane of the cross-section and flexible in the direction of the cylinder axis, i.e. no in-plane deformation of the cross-section was allowed. In addition to the axial springs, rotational springs with flexibility around the circumference were included, while rotations in the radial and axial directions were restricted. In the finite element model these springs were attached to every boundary node around the circumference, 192 per edge. The springs are shown in figure 10.

The stiffness of the rotational springs was equal for all springs and independent of any degree of freedom, whereas the stiffness of the longitudinal springs depended on the sign of the spring deformation: in tension the spring stiffness was $k^+ = 1.72 \cdot 10^7 \mathrm{Nm}^{-1}$ and in compression the spring stiffness was $k^- = 1.19 \cdot 10^8 \mathrm{Nm}^{-1}$. These values were obtained with a least-squares fit of the test data using a simple spring model in Microsoft Excel. The compressive spring stiffness corresponded to the laminate stiffness of the cylinder and tab sections that were clamped between the end rings, confirming that the load was transferred through direct contact with the backplate. The load transfer on the tension side was less efficient than on the compression side, resulting in a significantly lower stiffness of the interface. A possible improvement of the interface model

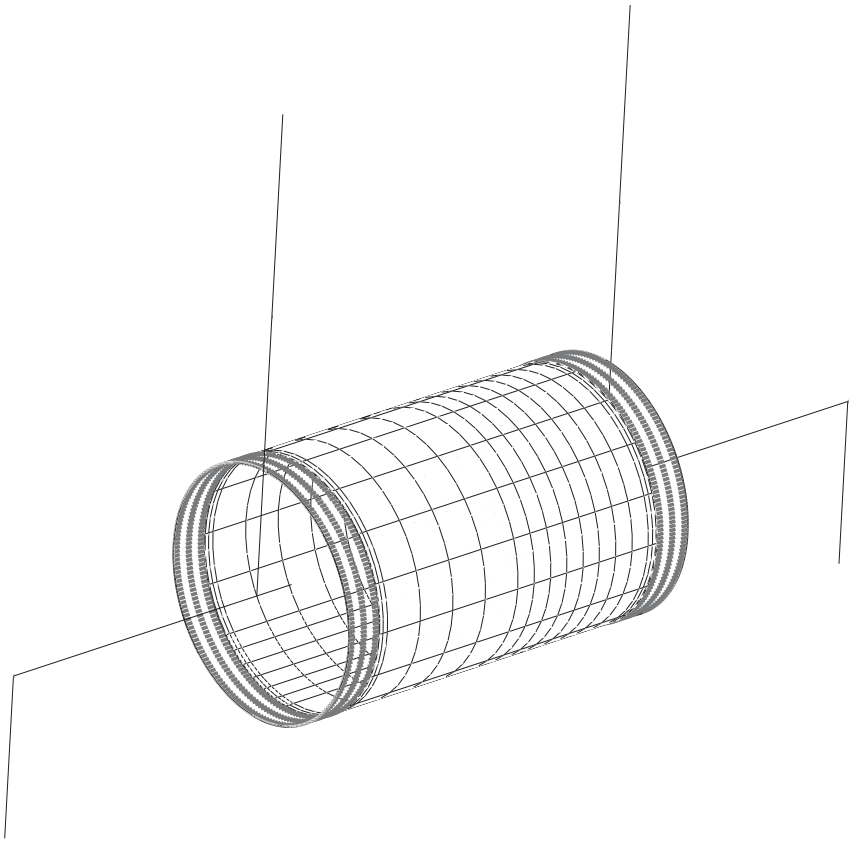

Figure 10. Finite element model including springs and test mechanism

could be obtained by designing and testing a small assembly that is representative of the interface, i.e. a piece of composite laminate which is attached to a backplate through two L-profiles using bolts and adhesive. Note: working to this level of detail was judged unnecessary for the current research.

The change in boundary conditions caused larger end rotations and a shift of the neutral axis, possibly causing changes in the behavior of the test mechanism. A simplified representation of the test mechanism was therefore added to the finite element model. The parts representing the test structure were rigid bodies, connected by hinges, with a rigid connection to the end plate. The test mechanism is shown in figure 10.

The results of the geometrically nonlinear finite element analysis including the boundary conditions and test mechanism as described above are also plotted in figure 9, where they are indicated by FE_f. The adjusted finite element results showed a good agreement with the experimental results.

C. Riks Analysis: FE Model Including Imperfections

One aspect that was not taken into account in the previous model, and that could have a large influence on the experimental buckling load of thin-walled cylindrical shells in compression was the presence of geometrical imperfections.

Geometric imperfections of cylindrical shells are expressed in terms of a deviation of the cylinder shape in radial direction when compared to the perfect cylinder, i.e.:

$$w = r - R \tag{3}$$

where w is the imperfection, r is the local radius and R is the perfect cylinder radius. The measured imperfections, which will be discussed in the results section, were included in the finite element model by specifying the value of w on each node. The ABAQUS **Imperfection* data card was used for this purpose. Subsequently a Riks analysis was performed to predict the mechanical behavior and the collapse load of the cylinder.[16,34–36] Cylinders with geometric imperfections do not always exhibit bifurcation buckling, but can

gradually form buckles and become unstable. The load at which this occurs is also referred to as the collapse load.

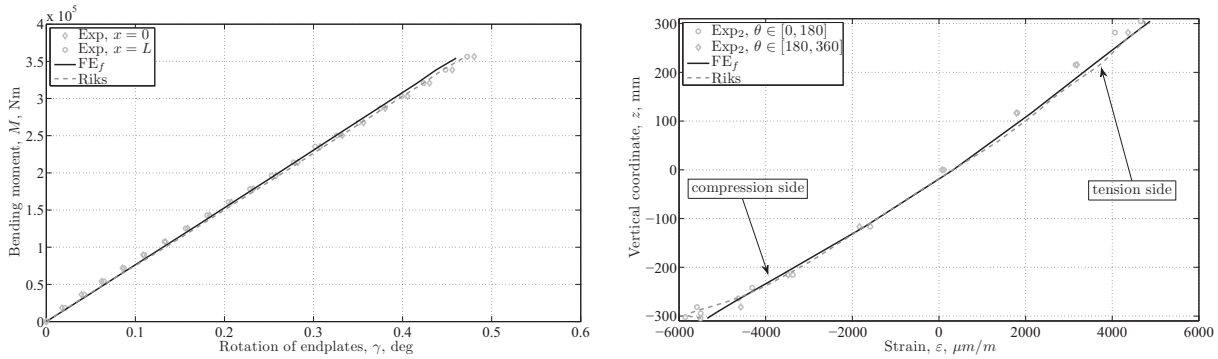

(a) Global response

(b) Strain distribution at M=356 kNm

Figure 11. Comparison baseline test and FE predictions with and without imperfections

The moment-rotation curves for the nonlinear static analysis without imperfections and the Riks analysis with imperfections are given in figure 11(a). Including imperfections had little influence on the shape of the load-deflection curve, but a large influence on the predicted collapse/buckling load. The collapse load predicted by the Riks analysis was 488 kNm, whereas the model without imperfections predicted a buckling load of 570 kNm. The inclusion of imperfections in the analysis also improved the agreement between the analytical strain distribution and the experimental strain distribution on the compression side, as shown in figure 11(b).

V. Results

The test results for 3 test configurations will be presented and compared in this section. The first test configuration is the bending test of the baseline cylinder. The second test configuration is the bending test of the variable-stiffness cylinder in the orientation for which it was optimized. The cylinder had a high axial laminate stiffness at $\theta = 0\,^\circ$ and a low laminate stiffness at $\theta = 180\,^\circ$, which are the respective tension and compression side of the cylinder in this configuration. In the third test configuration the variable-stiffness cylinder was rotated 180 $^\circ$ about the longitudinal axis, such that the loading on the cylinder was reversed compared to configuration 2. Consequently, the low-stiffness part of the cylinder in configuration 3 was in tension and the high-stiffness part of the cylinder was in compression. In the remainder of this paper the second configuration will be referred to as the variable-stiffness cylinder in the *preferred* orientation, while the third configuration will be referred to as the variable-stiffness cylinder in the *reversed* orientation.

The experimental results are compared to the results of the finite element predictions using the Riks analysis, including the flexible boundary conditions and the test mechanism.

A. Global Response

The global response of a cylinder loaded in bending is characterized by the moment-rotation curve. The moment-rotation curves for the baseline (subscript b) and the variable-stiffness cylinder in the preferred orientation (subscript p) and reversed orientation (subscript r) are given in figure 12. The experimental results are denoted "Exp" and the finite element predictions are denoted "Riks".

A good agreement between the experimental results and the analytical prediction was found for all configurations. The global stiffness of the variable-stiffness cylinder was larger than that of the baseline cylinder, because 3/4 of the variable-stiffness cylinder had a higher laminate stiffness than the baseline cylinder, as was shown in figure 3(a).

The initial bending stiffness of the variable-stiffness cylinder was equal for both cylinder orientations, but a small difference arose at higher loads: the response was less stiff when the cylinder was loaded in the preferred orientation than when it was mounted in the reversed orientation. This difference was attributed to the influence of the boundary conditions, because the measured end rotation included both the deformation of the cylinder and the deformation of the cylinder-structure interface. The interface on the tension side

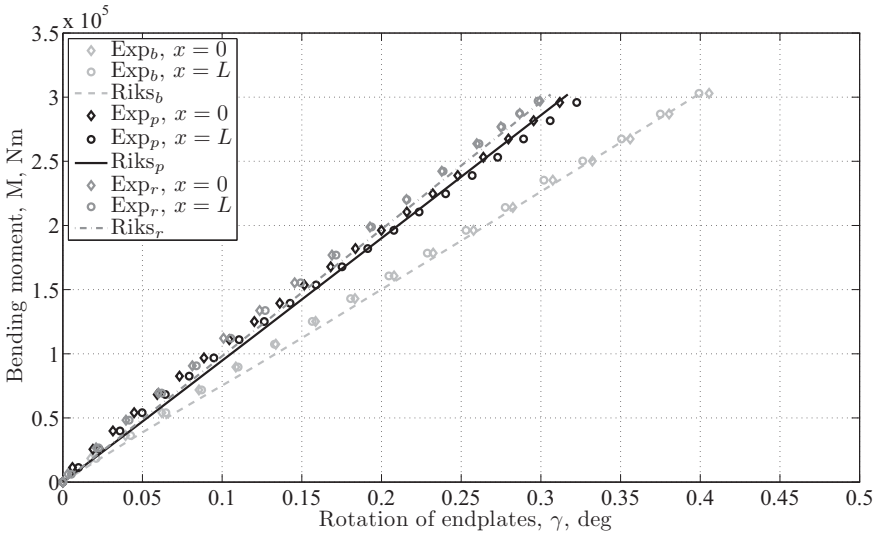

Figure 12. Moment-rotation curves

was a factor 7 more flexible than the interface on the compression side and therefore the deformation of the interface on the tension side dominated the amount of end rotation. The stiff part of the laminate ($\theta = 0\,^\circ$) in the preferred orientation was loaded in tension, requiring high loads to be transferred through the cylinder-structure interface. The tension side of the cylinder carried smaller loads when the cylinder was oriented in the reversed orientation and therefore smaller tensile loads needed to be transferred by the cylinder-structure interface of the variable-stiffness cylinder in this orientation. As a consequence, the deformations of the interface on the tension side, and thus the overall end rotations, were smaller for the reversed cylinder orientation than for the preferred orientation.

B. Geometric Imperfections

The measured geometric imperfections will be discussed in this section, this is because the other results such as strain data and cylinder buckling predictions are influenced by the geometric imperfections. Geometric imperfections are usually expressed in terms of a deviation from the perfect cylinder radius. A positive imperfection value signifies a radius that is larger than the perfect radius and a negative imperfection value indicates a radius that is smaller. Mathematically the imperfection w is given by Eq. 3.

The geometric imperfections of the baseline and the variable-stiffness cylinder were measured using the digital image correlation system. The data was collected by taking pictures at different locations around the circumference of the cylinder with a stereo camera system and by assembling them into one data set covering the full cylinder using VIC3D software. A least-squares fit was applied to determine the location and orientation of the cylinder axis and the geometric imperfections were calculated with respect to this best-fit axis.

The geometric imperfections for the baseline cylinder are depicted as contour plot on the expanded cylinder surface in figure 13. The maximum imperfection was 1.5 mm, approximately 35 percent of the wall thickness. The shape of the imperfect cylinder was oval with little lengthwise variation. Looking at the lengthwise imperfection at a local level, however, many little variations in radius could be observed, which can be seen as local waviness in the laminate. These small imperfection variations may have been caused by the bagging process.

The imperfection distribution of the variable-stiffness cylinder is given in figure 14. A comparison of the shape and magnitude of the imperfection distribution with those of the baseline cylinder in figure 13 showed that the absolute values of the imperfections were in the same range and that the shape was very similar. The global imperfection shape was therefore expected to be tool related. Unfortunately, the cylinders were not marked such that the part orientations could be traced back to the tool orientation. The shapes of the imperfection distribution might match if the x-direction of the baseline cylinder plot was reversed and if the pattern was shifted 90 degrees in the positive $\theta-$direction. It would be interesting either to measure

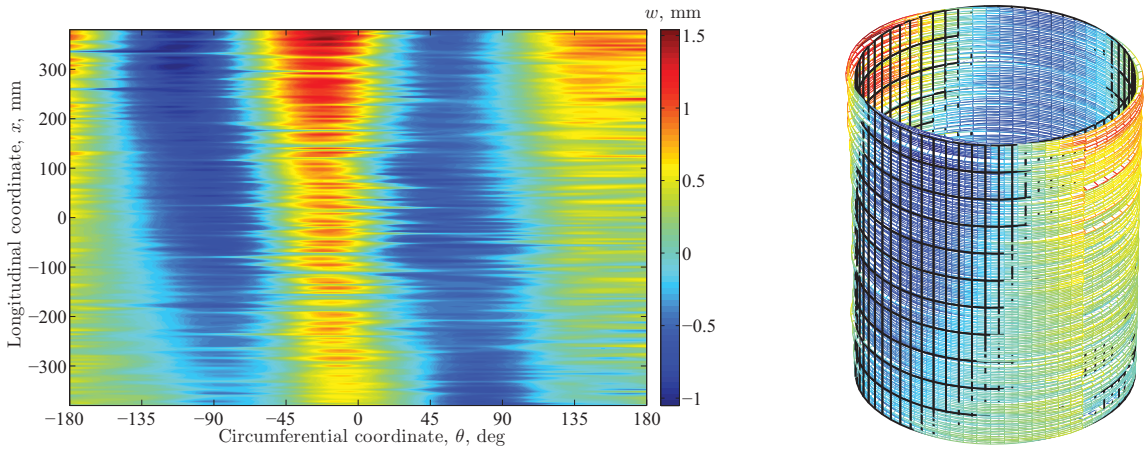

(a) Mapping of imperfections

(b) 20 times magnified

Figure 13. Geometric imperfections, w, of the baseline cylinder

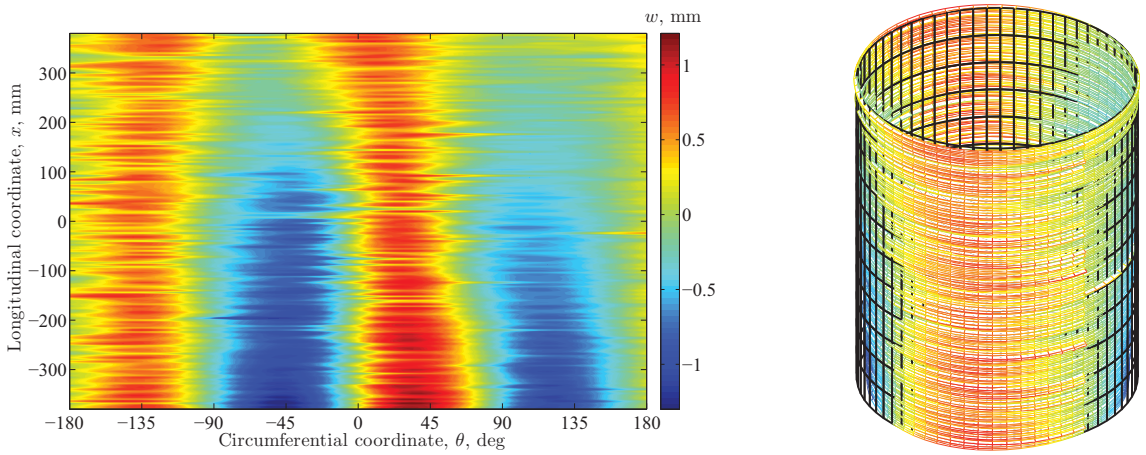

(a) Mapping of imperfections

(b) 20 times magnified

Figure 14. Geometric imperfections, w, of the variable-stiffness cylinder

the mandrel or to build and measure more cylinders manufactured on the same mandrel to check if the imperfections are indeed tool related.

The magnitude of the imperfections of the variable-stiffness cylinder were surprisingly in the same range as those of the baseline cylinder, although the varying fiber orientations, and consequently the varying coefficients of thermal expansion, were expected to have caused larger imperfections. The constraints on the laminate stiffness that were applied in the design excluded extreme stiffness variations and thereby also limited the variation in coefficients of thermal expansion. This could explain that the shape and magnitude of the variable-stiffness cylinder were similar to those of the baseline cylinder. A detailed finite element analysis of the part during curing including cool-down effects such as thermal expansion, chemical shrinkage and tool-part interaction could shed more light on the effect of varying fiber orientations on the final part shape. Furthermore, the imperfections were measured after the steel tabs were bonded to the surface and after the holes at the cylinder ends were drilled. These operations could also have influenced the final shape of the parts.

C. Strain Gauge Results

Each cylinder was populated with 113 strain gauges, mostly on the outer surface of the cylinder, see figure 8. An overview of the data collected by these strain gauges will be given below.

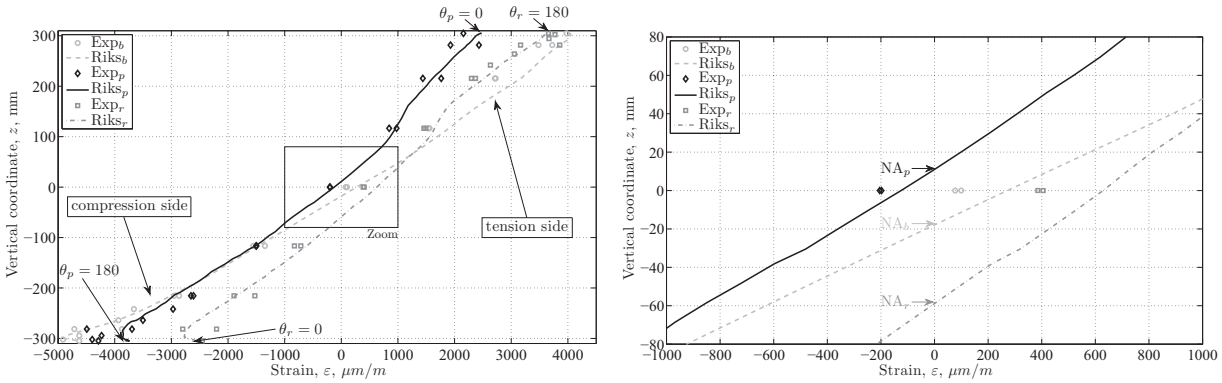

(a) Full cross-section

(b) Zoom around neutral axis

Figure 15. Axial strain distribution with $z-$coordinate of the cylinder at 302 kNm compared to the Riks analysis

The axial strains measured by the series of strain gauges halfway the length of the cylinder ($x = 394$ mm in figure 8) are plotted as a function of the vertical coordinate z in figure 15. The strains predicted by the finite element model are also plotted in figure 15. The distribution is given for a bending moment of 302 kNm, which was the maximum load to which the variable-stiffness cylinder was loaded in the reversed orientation. The baseline results are shown by the light gray circles and the dotted line, the black diamonds and the continuous line represent the variable-stiffness cylinder in the preferred orientation and the dark gray squares and the dash-dot line give the results for the variable-stiffness cylinder in the reversed orientation. Again a good agreement between the experimental and analytical results of the Riks analysis was found. The baseline strain distribution showed a small shift of the neutral axis in negative $z-$direction, caused by the stiffer boundary conditions on the compression side. These same boundary conditions caused a small difference in the maximum tensile and compressive strain values of the baseline cylinder, which would have been the same for perfectly clamped boundary conditions. The neutral axis of the variable-stiffness cylinder in the preferred orientation was shifted in the positive direction, this was because the laminate stiffness on the tension side was almost twice as stiff as the laminate stiffness on the compression side. The difference in stiffness also resulted in much lower strains on the tension side than on the compression side, despite the fact that higher loads were carried on the tension side, see figure 16. The high-stiffness part of the laminate became the compression side when the orientation of the variable-stiffness cylinder was reversed, while the low-stiffness part of the laminate became the tension side. The higher stiffness of the laminate and the boundary conditions on the compression side were mutually reinforced, such that the neutral axis shifted below that of the baseline cylinder.

The shift in neutral axis also influenced the extreme strain values, and reversing the cylinder orientation did not result in a reversal of the strains. The influence of the boundary conditions becomes more apparent when the strain distribution of the Riks analysis is compared to that of a nonlinear finite element analysis with clamped boundary conditions without any imperfections, as shown in figure 17. The axisymmetric and clamped boundary conditions resulted in a reversal of the strains in the variable-stiffness cylinder when the cylinder orientation was reversed. The $\theta = 0\,^\circ$ and $\theta = 180\,^\circ$ locations have been marked for both variable-stiffness cylinder orientations in figure 17(a). The strain for the reversed orientation at $\theta = 0\,^\circ$ was exactly the negative of the strain at $\theta = 0\,^\circ$ in the preferred orientation. The same was true for the $\theta = 180\,^\circ$ location. The locations of the neutral axes in figure 17(b) were also reversed. The shift of the neutral axis of the baseline cylinder was negligible and the neutral axis of the variable-stiffness cylinder in the preferred orientation in positive z direction was equal to the shift of the reversed orientation in negative z direction. Reviewing the strain results of the experiment and the Riks analysis of figure 15 shows that at $\theta = 0\,^\circ$ the tensile strain of the variable-stiffness cylinder in the preferred orientation was smaller than the compressive strain at $\theta = 0\,^\circ$ in the reversed orientation. This was caused by the shift of the neutral axis due to the non-symmetric boundary conditions. The same phenomenon can be observed at $\theta = 180\,^\circ$.

The strain values of the baseline cylinder at both the extreme tension side ($z > 200$ mm) and the extreme compression side ($z < 200$ mm) exceeded the strain values of the variable-stiffness cylinder in either orientation. Strength constraints in the aerospace industry are often based on maximum strain values, which means that the variable-stiffness cylinder would have an advantage over the baseline cylinder, because the

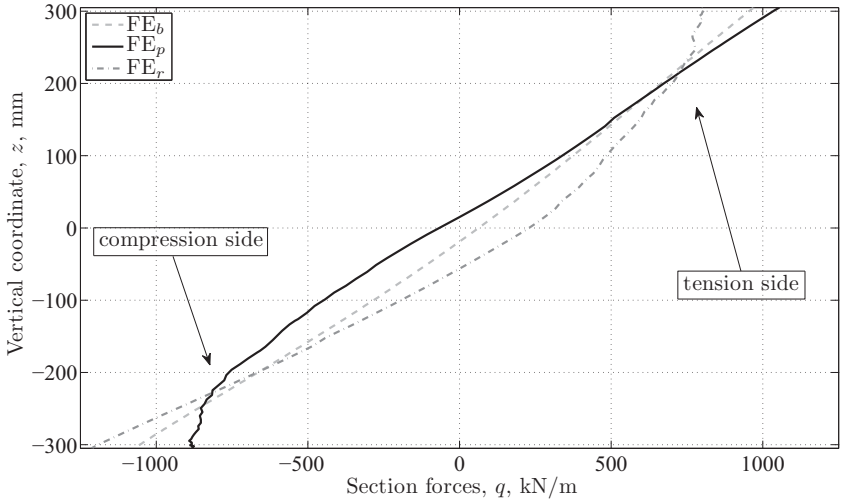

Figure 16. Distribution of axial loads with $z-$coordinate of the cylinder at 302 kNm

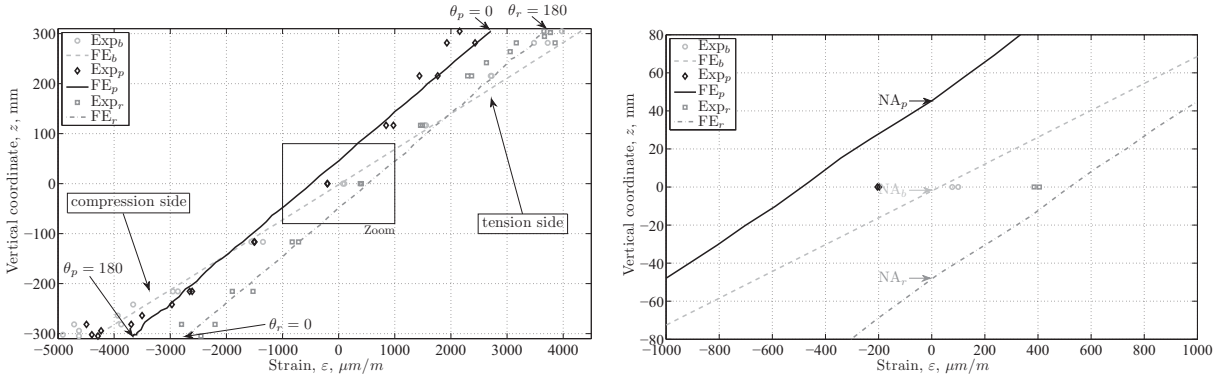

(a) Full cross-section

(b) Zoom around neutral axis

Figure 17. Axial strain distribution with $z-$coordinate of the cylinder at 302 kNm compared to the nonlinear FEA with clamped boundary conditions

strain values were smaller at equal load levels. The strains of the variable-stiffness cylinder between $\theta = 135\,^\circ$ and $\theta = 225\,^\circ$ were smaller than the strains of the baseline cylinder, even though the stiffness of the baseline cylinder at this location was larger. This is because the stiffer side of the cylinder carried higher loads and reduced the load on the other side of the cylinder, as can be seen in figure 16. The tension side ($z >$ 200 mm) of the variable-stiffness cylinder in the preferred orientation carried higher loads than the baseline and also the area close to the neutral axis (-220 mm $< z <$ 20 mm) was more effective at carrying compressive loads, so that the compression side ($z <$ -220 mm) carried significantly lower loads. The idea behind the improved performance was the same as predicted by the linear finite element model with clamped boundary conditions, despite the differences caused by the flexible boundary conditions. The loads carried on the compression side of the variable-stiffness cylinder in the preferred orientation were lower than those of the baseline cylinder, which resulted in an ability to carry a higher bending moment before buckling occurred. The effect for the variable-stiffness cylinder in the reversed orientation was just the opposite: higher loads were carried on the compression side, thereby reducing the buckling load compared to the baseline cylinder. The presentation and the discussion of the numerical results for the buckling loads will be dealt with at the end of this section.

D. Digital Image Correlation Results

The disadvantage of measuring strains with strain gauges, as described above, is that strain gauges only provide point data. This makes it difficult to form a complete picture of the strain field based on strain gauge data. A digital image correlation (DIC) system can provide this kind of information by extracting the deformation field from the digital images and subsequently calculating the strain field. The strains measured by the DIC system were compared to the strains of two neighboring strain gauges which were located at the same circumferential coordinate to serve as a reference for the accuracy of the DIC system. The data points were picked as close to the symmetry plane as possible to minimize the effect of the boundary conditions. These values are listed for the circumferential locations $\theta = 0\,^\circ$, $\theta = 180\,^\circ$, $\theta = 225\,^\circ$, $\theta = 270\,^\circ$ and $\theta = 315\,^\circ$ in table 2 and show a good agreement between the two measurement methods.

Table 2. Comparison of strains measured with strain gauges and DIC at maximum load

$\theta = 0\,^\circ$		$\theta = 180\,^\circ$		$\theta = 225\,^\circ$		$\theta = 270\,^\circ$		$\theta = 315\,^\circ$	
x	ε	x	ε	x	ε	x	ε	x	ε
mm	μm/m	mm	μm/m	mm	μm/m	mm	μm/m	mm	μm/m
394	5329	394	-6409	394	-4349	394	100	394	3677
489	5326	489	-6490	584	-4252	584	55	584	3759
DIC	5258	DIC	-6477	DIC	-4323	DIC	52	DIC	3822

The DIC results for the compression side of the baseline cylinder and the variable-stiffness cylinder in the preferred orientation are plotted in figure 18. The longitudinal strains are superimposed on a picture of the speckled cylinder surface. The areas with wires were omitted from the analyzed area because correlation across wires gives unreliable results. The figures show an area that covers a section of approximately 110 degrees of the cylinder. The wires on the lower side of the figure were located on the $\theta = 180\,^\circ$ line of the cylinder, which was the compression side. The wires on the top of the figure were located at $\theta = 270\,^\circ$, close to the neutral axis. Strain concentrations can clearly be observed at the boundaries of both cylinders, most pronounced close to the $\theta = 180\,^\circ$ location, whereas the strain field at the center of the cylinder was undisturbed. It was not possible to draw any conclusions about the dispersion of the edge effects based on the data from the strain gauges, while the boundary effects are clearly visible using the DIC system. Comparing the strain distribution of the baseline cylinder with that of the variable-stiffness cylinder again confirmed the findings discussed in the previous section, namely that overall the strains in the variable-stiffness cylinder were lower and that the neutral axis ($\varepsilon = 0$) was shifted upward because of the stiffness variation.

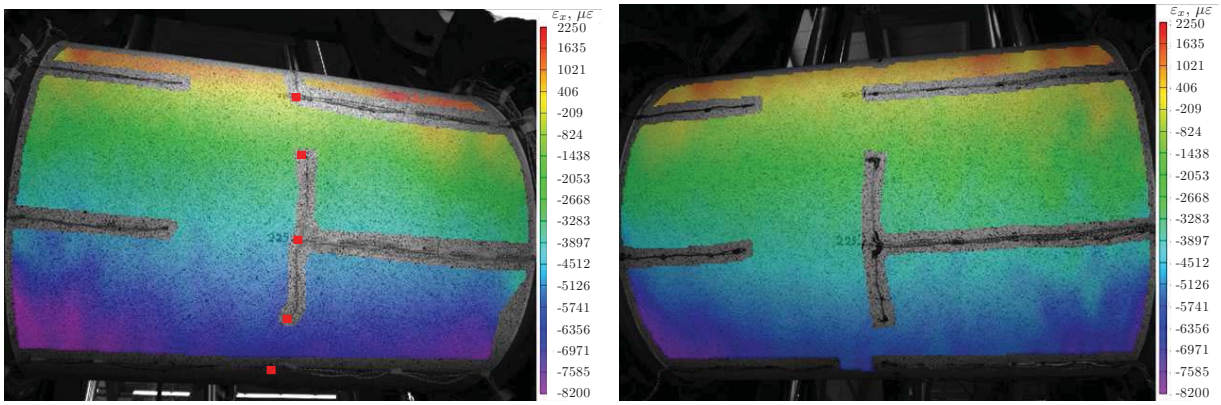

(a) Baseline cylinder (b) Variable-stiffness cylinder, preferred orientation

Figure 18. Strains on the compression side of the baseline and VS cylinder at M = 415 kNm

The strains predicted by the Riks analysis on the compression side of the baseline cylinder are shown in figure 19. Part of the contour was made white to indicate that this area was outside the field of view of the DIC measurements. The red squares indicate the location of strain gauges. The strain gauge at the bottom of the figure was located at $\theta = 180\,^\circ$ and the top strain gauge was located at the neutral axis at $\theta = 270\,^\circ$. These locations correspond to the wire locations shown in figure 18. A comparison of the strain field of the DIC measurements of figure 18(a) with the strains that were predicted with the ABAQUS model showed good agreement. Irregular strain patterns can be seen in both the measured and the analytical results, these

were caused by geometric imperfections. These variations in strain were also seen in the strain gauge data. The boundary condition effects were not captured by the finite element model.

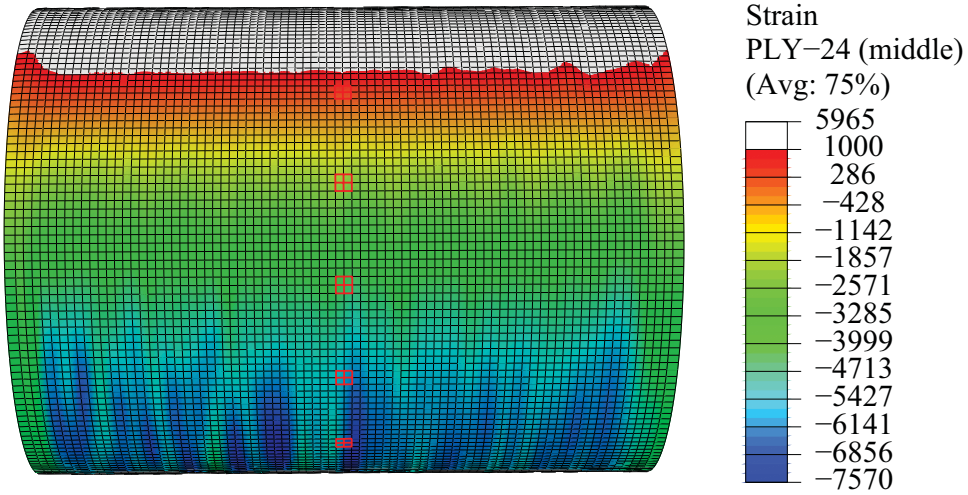

Figure 19. Predicted strains on the compression side of the baseline cylinder at M = 415 kNm

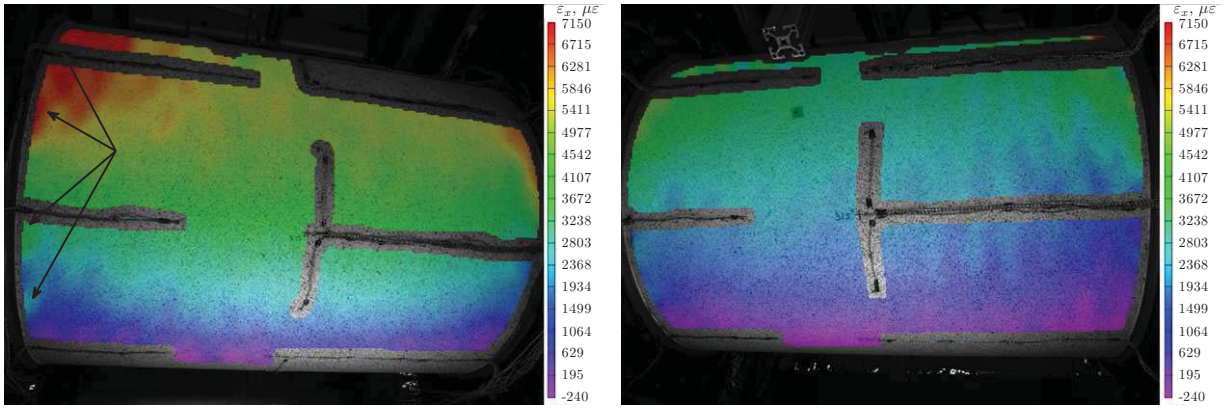

(a) Baseline, 415 kNm

(b) Variable-stiffness, preferred, M = 415 kNm

Figure 20. Strains on the tension side of the baseline and VS cylinder

The strains on the tension side of the cylinder are shown in figure 20. The wires located on the top of the figures indicate the $\theta = 0\,^\circ$ location, while the two other lines of wires are located at $\theta = 315\,^\circ$ and at the neutral axis, $\theta = 270\,^\circ$. Boundary condition effects can again be observed, but this time the higher strain regions are more concentrated. Some of these sites are indicated by arrows in figure 20(a). These strain concentrations were caused by the load introduction through the bolted connection. This phenomenon was not observed on the compression side, because in compression the load was transferred by direct contact with the back plate, which is a more uniform type of load transfer. The stress concentration at $\theta = 0\,^\circ$ was most prominent, because this was where the highest loads were transferred.

E. Comparison of the Buckling Load Predicted by the Different Finite Element Models

The different finite element models that were used to predict the buckling load of the cylinders were discussed in section IV. It was concluded from that discussion that the boundary conditions and geometric imperfections played an important role in the correct prediction of mechanical responses and the buckling load. The buckling loads for the three cylinder configurations as predicted by the four finite element models are reported in table 3.

A comparison of the predictions for the variable-stiffness cylinder in the preferred orientation with the baseline cylinder showed that the buckling load of the variable-stiffness cylinder was about 18 percent higher

Table 3. Features of the different FE models and the predicted buckling moments

Finite element model					Predicted buckling moment		
FE Model number	Boundary conditions	Analysis type	Mechanism included	Imperfections included	Baseline M_{cr}, kNm	VS preferred M_{cr}, kNm	VS reversed M_{cr}, kNm
1	clamped	linear static	no	no	678	805	477
2	clamped	nlgeom static	no	no	647	763	470
3	flexible	nlgeom static	yes	no	570	671	430
4	flexible	static Riks	yes	yes	488	589	409

than that of the baseline cylinder, regardless of which model was used. The general mechanism of redistributing loads within the cylinder was not changed, although the boundary conditions did affect the load introduction. Therefore the buckling load of the variable-stiffness cylinder in the preferred orientation was still higher than that of the baseline cylinder and the buckling load of the variable-stiffness cylinder in the reversed orientation was still lower than that of the baseline. The decrease in buckling load for the preferred orientation of the variable-stiffness cylinder from model 1 to model 4 was 27 percent, which was similar to the baseline cylinder. The reduction for the variable-stiffness cylinder in the reversed orientation was only 16 percent. The reduction in buckling load from model 3 to model 4 was much smaller for the reversed configuration of the variable-stiffness cylinder than for the other baseline cylinder and the variable-stiffness cylinder in the preferred configuration. The only change from model 3 to model 4 was the inclusion of geometric imperfections in the model. The geometric imperfections of the variable-stiffness cylinder in the preferred and reversed direction were the same and thus it can be concluded that the location of the imperfections in relation to the loading direction were also important, because cylinder buckling is governed by imperfections on the compression side, whereas it is insensitive to imperfections on the tension side. The imperfections between $\theta = 90\,^\circ$ and $\theta = 270\,^\circ$ were important for the reversed cylinder configuration, whereas the imperfections between $\theta = 270\,^\circ = -90\,^\circ$ and $\theta = 90\,^\circ$ dominated the buckling behavior for the preferred configuration.

VI. Discussion and Outlook

A fixture was designed to test a cylinder with a diameter of 609 mm and a length of 990 mm in pure bending. Strains and displacements were measured using strain gauges, digital image correlation and LVDTs. Two carbon fiber-reinforced cylinders were tested: one with a baseline laminate and one with circumferentially varying laminate stiffness. The variable-stiffness cylinder was tested in two configurations: one, it was tested in the orientation for which it was optimized, called the preferred configuration, and two, it was tested while rotated $180\,^\circ$ about the longitudinal axis, such that the loading on the cylinder was reversed, this was called the reversed configuration. This resulted in three test configurations: the baseline, the variable-stiffness in the preferred orientation and the variable-stiffness in the reversed orientation.

A comparison of the experimental response of the baseline cylinders with the finite element predictions revealed that the experimental boundary conditions were more flexible than originally modeled in the finite element model. The introduction of flexible boundary conditions in the finite element model resulted in a good agreement between the experimental and the analytical results. A final improvement of the finite element predictions was achieved by including geometric imperfections in the model and by performing a Riks analysis. The latter model was used to make a prediction for the variable-stiffness test results.

A comparison of the experimental results with the finite element predictions of the Riks analysis in general showed a good agreement for all three configurations. The match of the end rotations and strains was equally good for the variable-stiffness cylinder and the baseline cylinder. The variable-stiffness cylinder was stiffer than the baseline cylinder when comparing the global behavior in terms of end rotations, which was to be expected because of the larger laminate stiffness of the variable-stiffness cylinder. The variable-stiffness cylinder response was stiffer in the reversed orientation than in the preferred orientation due to the boundary condition effects. The most important observation resulted from the strain distribution with the vertical coordinate of the cylinder: at equal load level the maximum compressive strains of the variable-stiffness cylinder in the preferred orientation were about 10 percent lower than those of the baseline cylinder; the tensile strains were 35 percent smaller. This difference in extreme strain values is a large improvement in performance when strain-based strength criteria are applied. In addition, the circumferential stiffness

variation resulted in a redistribution of the loads, such that the tension side was more effective in carrying loads, the compressive loads were carried by a larger part of the cylinder and the compressive load peak at $\theta = 180\,^\circ$ was significantly reduced compared to the baseline cylinder. The buckling load of the cylinder was increased by 18 percent as a result of this load redistribution. This improvement was maintained even when realistic boundary conditions and geometric imperfections were included.

In the future it would be interesting to include cutouts or damage in the cylinders to reduce the critical load and to make failure possible. The compression side of the cylinder would be the preferred location for the introduction of a defect, because normally the compression side of a cylinder in bending is the most critical part of the structure. Moreover, the load redistribution mechanism of the variable-stiffness cylinder should result in a higher load-carrying capability when compared to the baseline cylinder, even when cutouts or damage are introduced on the compression side.

References

[1]Blom, A. W., Stickler, P., and Gürdal, Z., "Optimization of a Composite Cylinder under Bending by Tailoring Stiffness Properties in Circumferential Direction," *Composites, Part B: Engineering*, Vol. 41, No. 2, 2010, pp. 157–165.

[2]Lorincz, J., "Composites Fly Lighter, Stronger," *Manufacturing Engineering*, Vol. 136, No. 3, 2006.

[3]Hyer, M. W. and Charette, R. F., "Use of Curvilinear Fiber Format in Composite Structure Design," *AIAA Journal*, Vol. 29, No. 6, 1991, pp. 1011–1015.

[4]Hyer, M. W. and Lee, H. H., "The use of curvilinear fiber format to improve buckling resistance of composite plates with central circular holes," *Composite Structures*, Vol. 18, No. 3, 1991, pp. 239–261.

[5]Nagendra, S., Kodiyalam, A., Davis, J. E., and Parthasarathy, V. N., "Optimization of Tow Fiber Paths for Composite Design," *Proceedings of the 36th AIAA/ASME/ASCE/AHS/ASC Structures, Structural Dynamics and Materials (SDM) Conference*, AIAA, New Orleans, LA, USA, 1995.

[6]Gürdal, Z. and Olmedo, R., "In-Plane Response of Laminates with Spatially Varying Fiber Orientations: Variable Stiffness Concept," *AIAA Journal*, Vol. 31, No. 4, 1993, pp. 751–758.

[7]Olmedo, R. and Gürdal, Z., "Buckling Response of Laminates with Spatially Varying Fiber Orientations," *Proceedings of the* 34th *AIAA/ASME/ASCE/AHS/ASC Structures, Structural Dynamics and Materials (SDM) Conference*, AIAA, 1993.

[8]Gürdal, Z., Tatting, B. F., and Wu, K. C., "Variable Stiffness Composite Panels; Effects of Stiffness Variation on the In-Plane Buckling Response," *Composites Part A-Applied Science and Manufacturing*, Vol. 39, No. 5, 2008, pp. 911–922.

[9]Tatting, B. F. and Gürdal, Z., "Design and Manufacture of Tow-placed Variable Stiffness Composite Laminates with Manufacturing Considerations," *Proceedings of the* 13th *U.S. National Congress of Applied Mechanics*, 1998.

[10]Wu, K. C. and Gürdal, Z., "Thermal Testing of Tow-Placed Variable Stiffness Panels," *Proceedings of the 42nd AIAA/ASME/AHS/ASC Structures, Structural Dynamics and Materials (SDM) Conference*, AIAA, Seattle, WA, USA, Apr 2001.

[11]Wu, K. C., Gürdal, Z., and Starnes, J., "Structural Response of Compression-Loaded, Tow-Placed, Variable Stiffness Panels," *Proceedings of the 43rd AIAA/ASME/AHS/ASC Structures, Structural Dynamics and Materials (SDM) Conference*, AIAA, Denver, CO, USA, Apr 2002.

[12]Tatting, B. F. and Gürdal, Z., "Analysis and Design of Tow-Steered Variable Stiffness Composite Laminates," *American Helicopter Society Hampton Roads Chapter, Structure Specialists' Meeting*, American Helicopter Society, Williamsburg, VA, USA, October 2001.

[13]Tatting, B. F. and Gürdal, Z., "Design and Manufacture of Elastically Tailored Tow Placed Plates," Tech. rep., Aug 2002, NASA/CR-2002-211919.

[14]Jegley, D. C., Tatting, B. F., and Gürdal, Z., "Optimization of Elastically Tailored Tow-Placed Plates with Holes," *Proceedings of the* 44th *AIAA/ASME/ASCE/AHS/ASC Structures, Structural Dynamics and Materials (SDM) Conference*, AIAA, Norfolk, VA, USA, Apr 2003.

[15]Lopes, C. S., Grdal, Z., and Camanho, P. P., "Variable-Stiffness Composite Panels: Buckling and First-Ply Failure Improvements over Straight-Fibre Laminates," *Computers and Structures*, Vol. 86, No. 9, 2008, pp. 897–907.

[16]ABAQUS, Inc., *ABAQUS Version 6.7 User's Manual*, Pawtucket, RI, USA, 2005.

[17]Lopes, C. S., Camanho, P. P., Gürdal, Z., and Tatting, B. F., "Progressive Failure Analysis of Tow-Placed, Variable-Stiffness Composite Panels," *International Journal of Solids and Structures*, Vol. 44, No. 25-26, 2007, pp. 8493–8516, 10.1016/j.ijsolstr.2007.06.029.

[18]Jones, S. E. and Platts, M. J., "Using internal fibre geometry to improve the performance of pin-loaded holes in composite materials," *Applied Composite Materials*, Vol. 3, No. 2, 1996, pp. 117–134.

[19]Tosh, M. W. and Kelly, D. W., "On the design, manufacture and testing of trajectorial fibre steering for carbon fibre composite laminates," *Composites Part a-Applied Science and Manufacturing*, Vol. 31, No. 10, 2000, pp. 1047–1060.

[20]Li, R., Kelly, D., and Crosky, A., "Strength improvement by fibre steering around a pin loaded hole," *Composite Structures*, Vol. 57, No. 1-4, 2002, pp. 377–383.

[21]Li, R., Kelly, D., Arima, S., Willgoss, R., and Crosky, A., "Fiber Steering around a Cutout in a Shear Loaded Panel," *Proceedings of the SAMPE 2002 Conference*, Long Beach, CA, USA, 2002.

[22]Huang, J., Haftka, R. T., and Rapoff, A. J., "Optimization Design of Composite Plates With Holes for Increased Strength," *Proceedings of the* 44th *AIAA/ASME/ASCE/AHS Structures, Structural Dynamics, and Materials (SDM) Conference*, AIAA, Norfolk, VA, USA, 2003.

[23]Huang, J. and Haftka, R. T., "Optimization of fiber orientations near a hole for increased load-carrying capacity of composite laminates," *Structural and Multidisciplinary Optimization*, Vol. 30, No. 5, 2005, pp. 335–341.

[24]Alhajahmad, A., Abdalla, M. M., and Gürdal, Z., "Design Tailoring for Pressure Pillowing using Tow-Placed Steered Fibers," *AIAA Journal of Aircraft*, Vol. 45, No. 2, 2008, pp. 630–640.

[25]Alhajahmad, A., Abdalla, M. M., and Gürdal, Z., "Optimal design of tow-placed fuselage panels with cutouts for maximum strength and buckling performance," *Proceedings of the 2nd International Conference on Multidisciplinary Design Optimization and Applications*, Gijon, Spain, 2008.

[26]Alhajahmad, A., Abdalla, M. M., and Gürdal, Z., "Optimal Design of a Pressurized Fuselage Panel with a Cutout Using Tow-Placed Steered Fibers," *Proceedings of the International Conference on Engineering Optimization*, Rio de Janeiro, Brazil, June 2008.

[27]Sun, M. and Hyer, M., "Use of Material Tailoring to Improve Buckling Capacity of Elliptical Composite Shells," *AIAA Journal*, Vol. 46, No. 3, 2008, pp. 770–782.

[28]Tatting, B. F., *Analysis and Design of Variable Stiffness Composite Cylinders*, Ph.D. thesis, Virginia Polytechnic Institute and State University, Oct 1998.

[29]Wu, K. C., "Design and Analysis of Tow-Steered Composite Shells using Fiber Placement," *Proceedings of the American Society for Composites 23rd Technical Conference*, DEStech Publications, Inc., Memphis, TN, USA, 2008.

[30]Wu, K., "Design and Manufacturing of Tow-Steered Composite Shells Using Fiber Placement," *50th AIAA/ASME/ASCE/AHS/ASC Structures, Structural Dynamics and Materials (SDM) Conference*, AIAA, Palm Springs, CA, USA, 2009.

[31]Blom, A. W., Tatting, B. F., Hol, J. M. A. M., and Gürdal, Z., "Path Definitions for Elastically Tailored Conical Shells," *Composites, Part B: Engineering*, Vol. 40, No. 1, 2009, pp. 77–84.

[32]Blom, A. W., Stickler, P. B., and Gürdal, Z., "Design and Manufacture of a Variable-Stiffness Cylindrical Shell," *Proceedings of the SAMPE Europe 2009 Conference*, SAMPE, Paris, France, March 2009.

[33]Blom, A. W., Rassaian, M., Stickler, P. B., and Gürdal, Z., "Modal Testing of a Composite Cylinder with Circumferentially Varying Stiffness," *Proceedings of the 50th AIAA/ASME/AHS/ASC Structures, Structural Dynamics and Materials (SDM) Conference*, AIAA, Palm Springs, CA, USA, May 2009.

[34]Riks, E., "An Incremental Approach to the Solution of Snapping and Buckling Problems," *Int. J. Solids Structures*, Vol. 15, 1979, pp. 529–551.

[35]Crisfield, M., "A Fast Incremental/Iterative Solution Procedure that Handles "Snap-Through"," *Computers and Structures*, Vol. 13, 1981, pp. 55–62.

[36]Powell, G. and Simons, J., "Improved Iteration Strategy for Nonlinear Structures," *International Journal for Numerical Methods in Engineering*, Vol. 17, 1981, pp. 1455–1467.